Article

Journal of the Brazilian Chemical Society

https://dx.doi.org/10.21577/0103-5053.20240138

J. Braz. Chem. Soc. **2024**, *35*, 12, e-20240138, 1-9

Why Ceria Nanoparticles Obtained from Ce-MOFs Exhibit Higher Catalytic Efficient in Soot Combustion? Understanding the Role of Intrinsic Properties of a Cerium-Organic Framework to Produce CeO_2

Viviane C. Gomes,[a] *Ayla Roberta Serra,*[b] *Gabriel C. de Sousa,*[a] *Cláudio Roberto Neri,*[a] *Baiwen Zhao,*[c] *Juliana F. de Lima,*[d] *Richard I. Walton*[c] *and Osvaldo Antonio Serra**[,a]

[a]*Laboratório de Terras Raras, Departamento de Química,*
Faculdade de Filosofia, Ciências e Letras de Ribeirão Preto (FFCLRP),
Universidade de São Paulo, 14040-901 Ribeirão Preto-SP, Brazil

[b]*Laboratório de Catálise Heterogênea, Universidade Federal de São Carlos, 13565-905 São Carlos-SP, Brazil*

[c]*Department of Chemistry, University of Warwick, Coventry CV4 7AL, UK*

[d]*Grupo de Materiais Fotoativos Nanoestruturados (FotoNano), Instituto de Química,*
Universidade Estadual do Rio de Janeiro, 20550-900 Rio de Janeiro-RJ, Brazil

Metal-organic framework (MOF) derivatives, such as porous metal oxides with controlled morphology have received great attention for applications in various fields. In this paper, the experimental results show that porous CeO_2 with high specific surface area (90.5 $m^2\ g^{-1}$) and nanorod morphology can be obtained by calcining a Ce-MOF template at optimized temperature (300-500 °C). The formation mechanism of this porous structure as well as the influence of the calcination temperature are well explained by taking into account thermal behavior and intrinsic structural features of the Ce-MOF precursor. We employed the oxides formed as heterogeneous catalysts to reduce the soot originating from the incomplete combustion of diesel or diesel/biodiesel blends. The CeO_2 materials exhibit outstanding catalytic activity, lowering the temperature of soot combustion from 610 to 370 °C. Compared with similar work, our catalyst exhibits enhanced soot oxidation activity, making it highly promising for diesel particulate filter applications. Such outstanding catalytic performance of the porous CeO_2 nanorods benefits from their large specific surface area, and morphological and structural characteristics.

Keywords: soot oxidation, cerium oxide, MOFs, ceria, catalysis

Introduction

Metal-organic frameworks (MOFs) are porous coordination polymers with highly crystalline networks fabricated by the formation of coordination bonds between organic ligands and inorganic metal ions.[1,2] Their unique properties, such as rationally designed structures, a large choice of morphologies, diverse dimensionality of porosity (1D, 2D and 3D) together with modifiable textural properties, make them excellent sacrificial templates and precursors to derive highly efficient nanocomposites.[3-5]

CeO_2 has been heavily researched due to its unique properties and potential applications[6-9] and it displays very high catalytic activity towards diesel soot oxidation.[10] Based on conditions and synthesis method, ceria nanostructures have been observed with different shapes such as nanoneedles,[9] nanowires,[11-14] nanorods,[15,16] nanotubes,[17,18] nanosheets[19] and nanospheres.[20] Much effort has been devoted to different synthesis methods for ceria nanostructures with tunable size and shape such as sol-gel,[21] hydrothermal,[22,23] pyrolysis,[21] sonochemistry,[24] and thermal decomposition.[25,26] Nanostructure plays an important role to modify the properties of oxides and is particularly relevant for catalysis. In the thermal decomposition of precursors, it is desirable to understand the parameters involved in these complex transformations and their influence on physical properties of the materials formed. Various studies[27-29]

---

*e-mail: osaserra@usp.br
Editor handled this article: Célia M. Ronconi (Associate)
Oswaldo always said that life can be hard, but Chemistry must always be "douce".

have demonstrated that pyrolysis temperature plays the most crucial role in optimization of desirable properties of MOF derivatives.

Considering that particulate matter is one of the major pollutants in diesel exhaust and directly implicated in respiratory and cardiovascular diseases in urban populations, it is mandatory to find strategies to reduce their emission.[30,31] Herein, we report the synthesis of a Ce-MOF and how CeO_2 nanoparticles can be obtained by pyrolysis at optimum temperatures (300-500 °C) under controlled conditions. We evaluated how the morphology and crystalline structure affected the catalytic soot efficiency, by the study of a mixture of CeO_2 and soot model (Printex-U®, Degussa),[6] using thermogravimetric analysis (TGA)/differential scanning calorimetry (DSC). This study provides new insights and improved understanding to rationally select the pyrolysis conditions to obtain optimized MOF-derived composites with desired properties for relevant applications.

Experimental

Materials

All chemicals used were analytical grade. Ultra-pure water was used for the preparation of all reagent solutions. The materials used for the synthesis of the Ce-MOF were purchased: cerium nitrate hexahydrate (($Ce(NO_3)_3\cdot6H_2O$, 99%, Fluka, St. Louis, USA) as the cerium precursor, benzene-1,3,5-tricarboxylic acid (H_3BTC, 98% Aldrich, China) as ligand precursor, and ethanol (CH_3CH_2OH, Sumaré, Brazil) as solvent from Êxodo Científica.

Synthesis of Ce-MOF

Ce-MOF was synthesized by a simple low temperature solvothermal method, similarly as described by Xiong *et al.*[32] 1.0 mmol of $Ce(NO_3)_3\cdot6H_2O$ was dissolved in 2.0 mL of ultrapure water (solution A); 1.0 mmol H_3BTC was dissolved in 18.0 mL of water-ethanol solution (v/v = 1:1) (solution B). Subsequently, solution A was added to solution B by dropwise with vigorous magnetic stirring and kept on a water bath at 50 °C. After continuing the process for 30 min, the precipitate was separated from the reaction mixture by centrifugation and washed several times with ethanol and ultrapure water, finally dried in an oven at 70 °C for 24 h.

Synthesis of CeO_2

The Ce-MOF was calcined at 300, 400, 500, 700, 900 °C for 2 h under air atmosphere, to produce porous ceria.

CeO_2 impregnation onto cordierite

The cordierite@Ce-MOF composites were obtained by immersing the cordierite substrate in a suspension of MOF precursor in ethanol under ultrasonication conditions. The cordierite was soaked in the precursor solution for 60 min, followed by drying under vacuum to obtain the cordierite@MOF composite. This procedure was repeated until a 10% increase in weight was observed. After that, the composite was heated for 2 h under the air atmosphere, in the chosen temperature. The cordierite was supplied by Umicore Brasil.

Characterizations

The samples were structurally characterized by powder X-ray diffraction (PXRD) on a D5005 diffractometer (Siemens AG Germany, now Bruker AXS GmbH, Karlsruhe Germany) operating with Cu Kα1/2 radiation (1.5418 Å, 40 kV, 30 mA) at 2° min^{-1} over the chosen angle range. Figure S1 (Supplementary Information (SI) section) confirmed the crystalline structure for the Ce-MOF, previously reported in the literature,[33] by comparison to the structure published for $La(BTC)\cdot6H_2O$ (CCDC 290771). Variable-temperature powder X-ray diffractometry was performed on a D8 diffractometer (Bruker AXS Ltd., Coventry, UK) operating with Cu Kα1/2 radiation. The diffractometer was equipped with a solid-state detector (VÅNTEC, Bruker AXS Ltd., Coventry, UK) and an XRK 900 reactor chamber (Anton Paar GmbH, Graz, Austria), allowing the sample to be heated from room temperature to 900 °C at intervals of 100 °C in flowing air.

The crystallite sizes and lattice parameters were estimated for the CeO_2 samples prepared from $Ce(BTC)\cdot6H_2O$. The average sample crystallite size was calculated by applying the Scherrer equation for the most prominent peak in the PXRD pattern, and the lattice parameters, Figure S2 (SI section) were determined by Rietveld refinement employing COD 9009008 as standard cubic CeO_2.

Raman analysis was performed on a handheld TacticID-GP Plus apparatus from B&W Tek (Metrohm, Shea Way Newark, DE, USA) with excitation source of 785 nm and laser power of 300 mW.

TGA was performed in a TA instruments model Q-600 analyzer operating in the simultaneous TGA-DTA-DSC modulus (Lukens Drive, New Castle, DE, USA), under synthetic air atmosphere, at a heating rate of 10 °C min^{-1}, from room temperature to 1000 °C. The thermogravimetric (TG) and differential thermal analysis (DSC) curves were acquired by using aluminum oxide (Al_2O_3) as an inert reference material. Figure S3 (SI section) confirmed the chemical formula Ce(BTC)·$6H_2O$. For the catalytic test, the soot and the catalyst (CeO_2) were mixed under tight contact condition at a catalyst/soot weight ratio of 9:1 and the mixture was placed in platinum crucibles and thermally treated.

N_2 adsorption-desorption isotherms at 77 K were measured with a NOVA 4200e Quantachrome (Boynton Beach, FL, USA) system. Before the adsorption isotherm was acquired, the calcined sample (0.15-0.17 g) was degassed at 150 °C for 3 h. The Brunauer-Emmett-Teller (BET) method was used to calculate the specific surface area of the sample. Pore size distribution was determined by applying the Barret-Joyner-Halenda (BJH) method to the desorption isotherms. The total pore volume was evaluated at $p/p_0 = 0.99$.

X-ray photoelectron spectroscopy (XPS) analyses were performed on a Scienta-Omicron ESCA+ spectrometer equipped with a high-performance hemisphere analyzer (EAC-2000 Sphere, Uppsala, Sweden) and a monochromatic radiation source Al Kα ($\eta\nu = 1486.6$ eV). The charging effect was suppressed by using a low energy electron flood gun. The analyses were performed in an ultra-high vacuum (UHV) environment (9-10 mbar). The obtained spectra were calibrated by using the adventitious carbon binding energy (284.8 eV) and fitted with a Gaussian-Lagrange function.

Morphology and particle size were examined with a scanning (FEG-SEM) (Mira 3, Tescan, Czech Republic) microscope. To improve the quality of the SEM images of the CeO_2 samples, they were coated on cordierite substrate, to validate the aspect of the samples that would be impregnated in cordierites in our future investigations for the required applications. A high vacuum mode energy-dispersive X-ray spectroscopy (EDS) analysis was carried out with an accelerating voltage of 20 kV and a work distance of 15 mm.

H_2 temperature-programmed reduction (H_2-TPR) investigations were carried out on a TPR/TPD Micromeritics AutoChem 2920 system (Micromeritics Instrument Corporation 4356 Communications Drive, Norcross, USA) that was fitted with a thermal conductivity detector. For the H_2-TPR experiments, the samples were pretreated up to 300 ºC (10 ºC min^{-1}) in air (50 mL min^{-1}) for 1 h, followed by an increase in temperature to 900 ºC (10 ºC min^{-1}) by employing 10% H_2/air flow (50 mL min^{-1}). Temperature-programmed desorption (TPD) was evaluated in a micro-reactor system coupled with a Pfeiffer Omni Star mass spectrometer, and the fragments m/z = 2 (H_2), 44 (CO_2), and 78 (benzene) were observed.

Results and Discussion

Figure 1a shows XRD patterns for ceria obtained from Ce-MOF calcined at different temperatures. The diffraction patterns for the catalysts are in accordance with typical face centered fluorite structure of CeO_2 (PDF number 34-394).[34] At low calcination temperatures XRD peaks are broad indicating low crystallinity. The diffraction peaks become sharper and stronger upon increasing the calcination temperature, showing crystalline growth.

X-ray powder thermodiffractometry was conducted for Ce-MOF from room temperature to 900 °C to investigate the behavior of cerium MOF during the transition from Ce(BTC)·$6H_2O$ to CeO_2, Figure 1b.The MOF structure remains stable from room temperature up to around 100 °C, beyond which it exhibits a transition to an amorphous material. This transition corresponds to the observed loss of water observed by TGA. CeO_2 crystallisation starts from 300 °C aligned to ligand combustion from the Ce-MOF seen in the TGA.

No significant variation in the lattice parameters (Table 1) was observed and all values are near to that

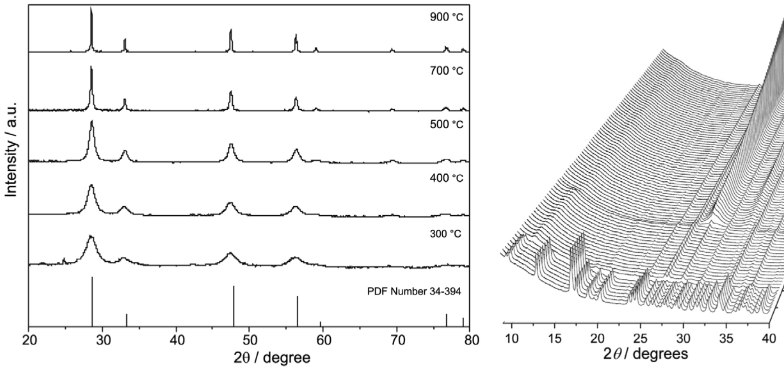

Figure 1. (a) Powder XRD patterns of the CeO_2 obtained under different temperatures calcination and (b) thermo powder XRD patterns for Ce-MOF up to CeO_2 formation.

Table 1. Lattice parameters and crystallite sizes for CeO_2 catalysts

Sample	Temperature / ºC	a / Å	Crystallite size / nm
CeO_2	300	5.423 ± 0.003	5.08 ± 0.10
	400	5.414 ± 0.002	7.16 ± 0.15
	500	5.417 ± 0.001	11.16 ± 0.12
	700	5.415 ± 0.0003	26.42 ± 0.38
	900	5.413 ± 0.0001	45.81 ± 3.26

reported for cubic ceria a = 5.41 Å.[34] Table 1 also shows that crystallite size increases with calcination temperature for all samples.

To evaluate the morphological properties of CeO_2, SEM micrographs of the cordierite substrate, raw and coated were acquired. Figure 2 shows the SEM micrographs of Ce-MOF and the derived CeO_2 materials. A large number of monodisperse nanorod particles are seen when the Ce-MOF was calcined between the range 300-500 °C (Figures 2b-2d), reflecting the morphology of the starting material (Figure 2a). When the temperature is above 500 °C, a mixture of nanorods and spherical morphologies (Figures 2e-2f) are seen, and also evidence of sintering, which increases according to high temperature of calcination.

The average diameter of the nanorods was 120-200 nm for the Ce-MOF and CeO_2 obtained between 300-400 °C. For CeO_2 obtained between 500-700 °C, the presence of spherical particles together with the nanorods is observed. In both cases, regular morphologies that are well dispersed on the surface of the cordierite ($Mg_2Al_4Si_5O_{18}$) are detected after the deposition of Ce-MOF and CeO_2. At the higher calcination temperature, spherically-shaped particles of CeO_2 can be found as the major component. Interestingly, for the samples prepared at lower temperature calcination, where the amorphous character is more intense, the morphology following the same of the starting MOF, suggesting that the morphology and structure is controlled by the decomposition temperature. The direct correlation is surprising good for catalysts with significantly different surface area.

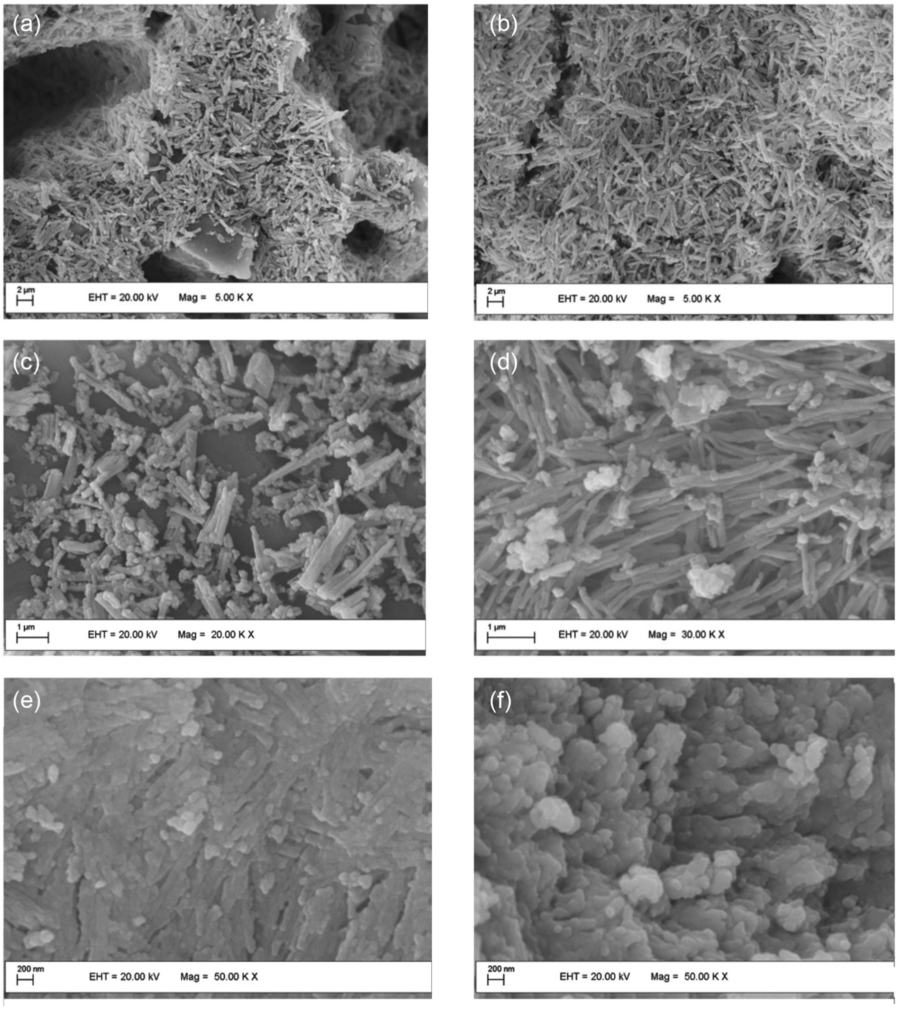

Figure 2. SEM micrographs of the (a) Ce-MOF, (b) CeO_2-300, (c) CeO_2-400, (d) CeO_2-500, (e) CeO_2-700, (f) CeO_2-900.

BET results of the catalysts are shown in Figure 3. CeO_2 obtained between 300-500 °C have a higher specific area when compared with CeO_2 700-900 °C. As shown in Table 2, CeO_2-400 presents high surface area (95.05 $cm^3\ g^{-1}$). At this point, it is important to mention that our aim is not seeking materials necessarily with high surface area, and CeO_2 was chosen due to it is morphological and redox properties, for being easy to prepare, and to the low-cost of the synthesis (when compared with other elements as Pt). However, the surface area is indeed more important for catalytic applications than redox properties. When the relative pressure p/p_0 was in the range of 0-0.6, the adsorption capacity of the catalysts increased slightly, indicating the existence of micropores. A rapid uptake was observed from 0.8 to 1.0, indicating mesopores structures.

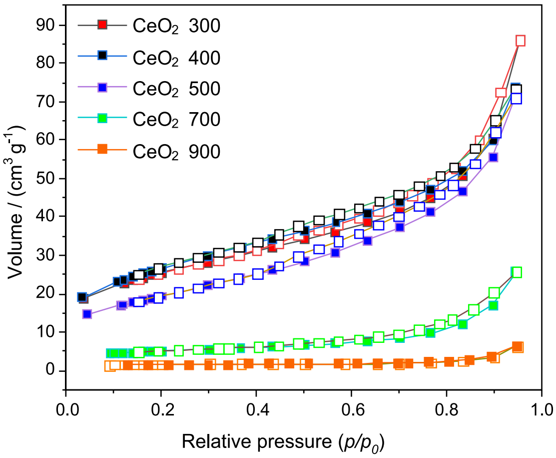

Figure 3. Nitrogen adsorption isotherms for ceria samples. Closed symbols represent adsorption and open symbols represent desorption.

Table 2. Specific surface area of the CeO_2 catalysts obtained by BET analysis

Sample	BET surface area / ($m^2\ g^{-1}$)	Porous volume / ($cm^3\ g^{-1}$)	Pore size / Å
CeO_2 300	90.32	0.128	69.5
CeO_2 400	95.05	0.108	54.8
CeO_2 500	69.01	0.114	61.6
CeO_2 700	17.20	0.039	97.3
CeO_2 900	5.43	0.009	126

H_2-TPR was employed to investigate the effect of thermal decomposition of the Ce-MOF on the reducibility of the CeO_2 catalysts. TPR profiles for CeO_2 samples are depicted in Figure 4. TPR profiles agree with those reported in the literature,[35-37] with two main features detected due to the reduction of ceria by H_2: one between 300 and 600 °C and the other between 650 and 900 °C. The peaks are related to the removal of surface (O_s) and bulk oxygen (O_b) ions, respectively. Table 3 summarizes the behavior of H_2 consumption by cerium oxides evaluated in this work. The samples calcined at 700 and 900 °C do not have reducible species on the surface, in agreement with the results described by Zhang *et al.*[36] who synthesized and calcined CeO_2 at different temperatures and found H_2 consumption similar values to those here reported.[37] They confirmed that increasing the calcination temperature reduces the surface area and increases crystallinity, resulting in less reducible oxygen species on the surface of the material. On the other hand, samples obtained by calcination at lower temperatures showed a higher H_2 consumption. According to Figure 4, the same was observed in this work. Furthermore, these materials showed a peak at low temperature in the H_2-TPD curves (150-200 °C), the peak also refers to the consumption of H_2, since it was also observed in the mass spectrometer ($m/z = 2$), Figure S4 (SI section). Reductions in this region are usually observed for noble metals or even for CeO_2 doped with noble or transition metals.[38,39] Organic residues (as carbon) from the composition of the original MOF could be retained on the surface of CeO_2, promoting some type of interaction that favors the consumption of H_2 and catalyst surface reduction. The TPR analysis indicates that the determining factor in the reduction of ceria is the loss of area due to the calcination temperature, a process that is increased by the textural and structural evolution and that promotes sintering, because of the specific area. The reducibility of ceria prepared using MOF as a precursor is significantly higher than that observed in CeO_2 prepared by other techniques, for example as compared to materials reported by Zhang *et al.*[40]

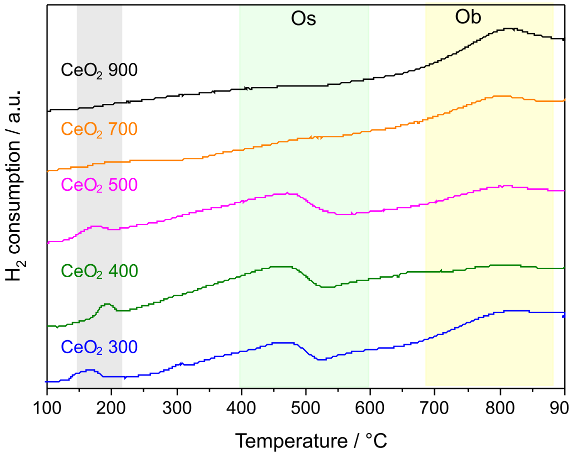

Figure 4. H_2-TPR profiles of CeO_2 obtained at different calcination temperatures. O_s and O_b refer to removal of surface and bulk oxide, respectively.

Raman spectroscopy provides identification of crystalline phases and corroborates the XRD observations. Figure 5 shows the full profile of CeO_2 catalysts. Figure 5a

Table 3. Total consumption of H_2 measured from ceria samples prepared from decomposition of Ce-MOF at different temperatures. O_s and O_b refer to removal of surface and bulk oxide, respectively

Peak region	Consumption of H_2 / (mmol g^{-1})				
	CeO_2-300	CeO_2-400	CeO_2-500	CeO_2-700	CeO_2-900
O_s peak	0.42	0.65	0.62	0.07	0.07
O_b peak	0.60	0.07	0.36	0.57	0.79

depicts a F_{2g} symmetric band around 463 cm^{-1} obtained from the space group O_h (*Fmm*) of a cubic fluorite structure and attributed to symmetrical stretching vibration of the $\{CeO_8\}$ units.[41] The broad profiles of the F_{2g} band for all CeO_2 samples suggest nanocrystalline particle sizes. Comparing ceria samples obtained at different temperatures, the F_{2g} band does not shift or broaden, which means that phonon lifetime and the presence of defects do not influence the spectra significantly. Furthermore, there is no broad band around 550-600 cm^{-1}, related to defects, according to the study of Loridant.[41] For the catalysts obtained after heat treatment above 400 °C a set of bands is observed between 1230-1800 cm^{-1}, Figure 5b, which can be attributed to molecular oxygen, carbon monoxide and carbon dioxide adsorbed on the ceria.[41]

XPS was employed to investigate the electronic surface properties before and after thermal decomposition of Ce-BTC, displayed in Figure S5 (SI section). The Ce 3d high resolution spectra are composed of multiplets from transitions to different final states.[42] The Ce-BTC without thermal treatment presents only Ce^{3+} peaks, labeled as v^0, u^0 v’ and u’ with respective binding energy 881.46, 899.82, 885.39 and 903.79 eV.[43] After thermal treatment, the Ce 3d spectra, also present an additional peak at 916.59 eV, attributed to u’’’ characteristic of Ce^{4+}, besides the new components v, u, v’’, u’’ and v’’’ at 882.65, 900.96, 888.65, 906.95 and 897.99 eV, respectively, also attributed to Ce^{4+}.[44,45] These results suggest an the oxidative process induced by thermal treatment, in accordance with the formation of CeO_2 demonstrated by XRD and Raman spectroscopy.

The oxidation of Ce-BTC by thermal treatment to CeO_2 can be estimated by the area ratio of the components associated with Ce^{3+} and Ce^{4+}, presented in Table S1 (SI section).[46,47] The composition of the surface of Ce-BTC after thermal treatment is mostly attributed to Ce^{4+} states, in a proportion higher than 90 atom%.

Although higher calcination temperatures favor higher proportions of Ce^{4+}, and O_2 adsorbed on ceria was observed through Raman for the samples obtained at higher temperatures (Figure 5b), only a small variation in the ratio Ce^{3+}/Ce^{4+} was observed. However, no influence in the soot catalytic activity can be inferred based on chemical states of cerium species existing on the surfaces of the ceria samples. The presence of Ce^{3+} in all materials must be highlighted, even in small quantities. We also believe that the presence of carbonate species on CeO_2 samples, as observed in the vibrational Raman analyses, may favor the concentration of Ce^{3+}, although the surface of CeO_2 is usually deficient in oxygen and Ce^{3+} is always seen.

Catalytic activity

We investigated catalytic soot combustion over the CeO_2 catalysts using Printex-U® as a soot model. The TGA curves showed the standard soot decomposition profile. The standard was completely oxidized at temperatures lower than ca. 610 °C (Figure S6, SI section). In the presence of CeO_2, the temperature at which combustion occurred decreased, according to the temperature that Ce-MOF was calcined. We observed, CeO_2 obtained between

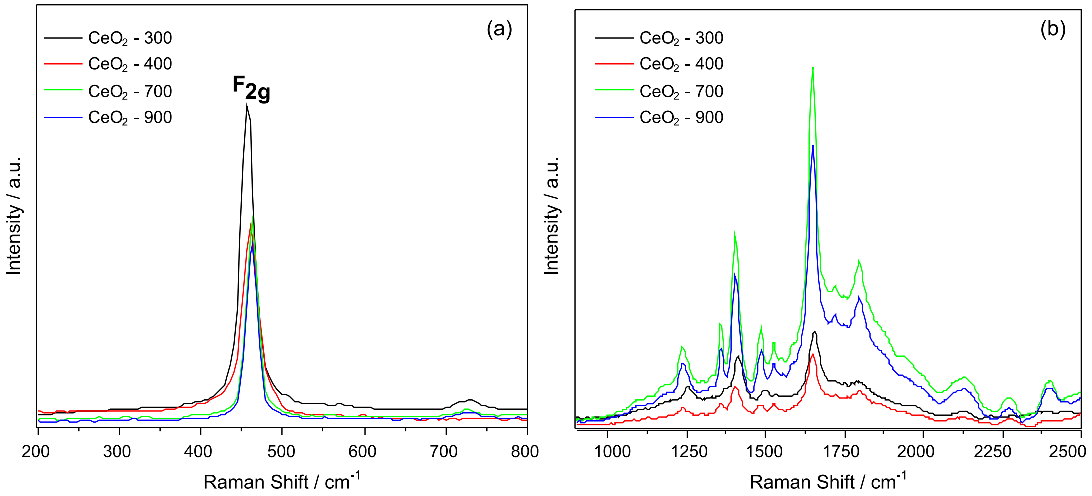

Figure 5. Raman spectra of CeO_2 (a) highlighted F_{2g} band and (b) zoom in from 900 to 2500 cm^{-1}.

300 and 500 °C showed excellent results, Figures 6 and S7 (SI section), with a significant lowering of the soot oxidation temperature. When CeO_2 was obtained at 700 and 900 °C, the catalytic efficiency was strongly diminished. When compared with other reports in the literature, it is possible to observe a huge difference in catalysis efficiency using CeO_2 obtained by sol-gel method and by MOF decomposition. In the first case the temperature is near 460 °C and, in this work, using MOF template, we managed to decrease the soot combustion temperature to 380 °C.[48] Table 4 lists the data of soot oxidation by reported Ce-containing catalysts reported in the literature. T_{50} is designated as the temperature at which 50% conversion of soot occurs during the experiment and T_{90}, sometimes denoted as T_m also, denoted the temperature of the peaks in soot oxidation curves. As shown, our result presents high catalytic efficiency, even if compared with doped ceria.

Table 4. Comparison reported of soot oxidation process using ceria-based catalysts, where T_{50} and T_{90} represent the temperature at which 50 and 90% conversion of soot occurs during the experiment

Catalyst	Morphology	T_{50} / °C	T_{90} / °C	Reference
CeO_2	spherical	455	520	48
CeO_2	nanorod	433	474	40
CeO_2	nanorod	402	450	49
CeO_2	nanorod	394	450	50
CeO_2	nanorod	456	494	51
Fe_5Ce_{95}	spongy	371	410	52
$Mn_{0.1}Ce_{0.9}O_y$	randomly aggregated	375	405	53
Ag-$Mn_{0.1}Ce_{0.9}O_y$	randomly aggregated	325	360	53
CeO_2	nanorod	360	400	this work

T_{50}: temperature at which 50% conversion of soot occurs during the experiment; T_{90}: temperature of the peaks in soot oxidation curves.

CeO_2-500 was submitted to catalytic soot combustion two further times to investigate the capability to reuse ceria catalysts. The first decomposition temperature was at 385 °C, followed by 394 °C, Table S2 and Figure S8 (SI section). The small variation observed indicates that thermal treatment did not affect the catalytic properties of cerium oxides. We have also conducted a MOF decomposition under argon atmosphere to evaluate any change in catalytic ability of CeO_2 obtained from MOFs. Ceria obtained in argon showed combustion temperatures 10-15 °C lower than CeO_2 calcined under air atmosphere (Figure S9, SI section). Although lower temperatures were observed, the variation is not significant to justify the

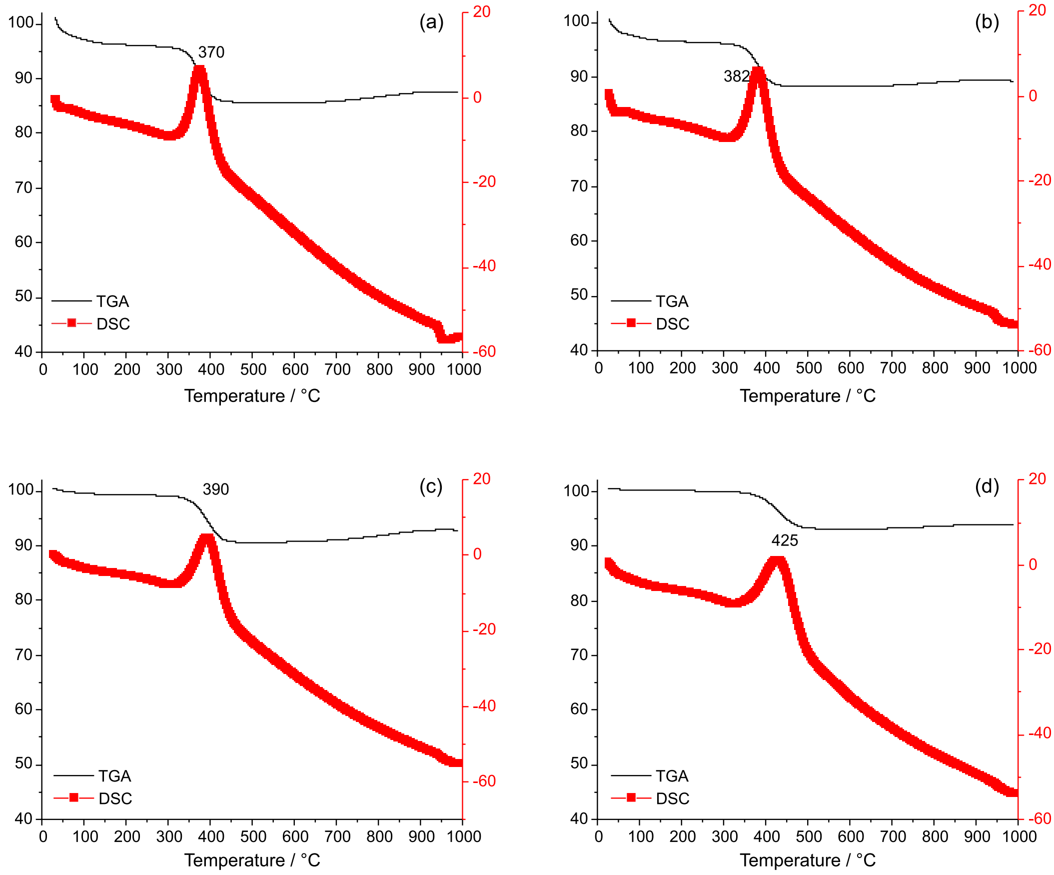

Figure 6. Differential thermal analysis (TGA-DTA) of CeO_2: (a) 400 °C, (b) 500 °C, (c) 700 °C, (d) 900 °C. All samples were mixed with Printex-U®.

employment of argon atmosphere during the calcination processes of MOFs.

Controlling the morphology of the nanoparticles can influence their catalytic performance because the different morphologies of the particles can expose different crystal faces. It is clear that CeO_2 nanorods are more active than CeO_2 nanospheres. For CeO_2 obtained between 300-500 °C, the soot combustion temperature was much lower when compared with CeO_2 700 and 900 °C, as shown in Figure 6. The catalytic oxidation over CeO_2 nanorods is therefore higher than that over nanospheres. Even after calcined in air at 500 °C for three times, the morphology of the nanorods remained unchanged and the activity decreased slightly.

Conclusions

CeO_2 nanoparticles have been prepared by a MOF decomposition procedure that effectively diminishes soot combustion temperature more efficiently than other ceria materials reported in the literature until now. The coexistence of Ce^{3+} and Ce^{4+} on the surface of the CeO_2 materials contributes to the catalysis properties, but it is not the primary way to explain the catalytic activity. The main differential of the new catalysts comes from their different crystal morphologies. The best results were obtained for CeO_2 from Ce-MOF calcined between 300-400 °C. It is coincident with change in structure, from amorphous to crystalline material, while the particle morphology is the same as the MOF starting material. With increasing decomposition temperature, we observe a higher crystallinity of the ceria obtained and a change in morphology, from nanorods to nanospheres. These variations decrease the efficiency of soot catalysis.

Supplementary Information

Supplementary information is available free of charge at http://jbcs.sbq.org.br as PDF file.

Acknowledgments

The authors acknowledge the National Council for Scientific and Technological Development-CNPq (426467/2018-3 and 432498/2018-4), and FAPESP (2018/07514-3 and 2021/14904-5), for financial support. We also thanks Fátima Zotin from from Universidade Estadual do Rio de Janeiro for the TPR and TPD analysis.

Author Contributions

Viviane C. Gomes was responsible for conceptualization, data curation, formal analysis; Gabriel C. de Sousa for formal analysis funding acquisition, investigation; Cláudio Roberto Neri for project administration, validation; Ayla Roberta Serra for investigation, project administration, writing original draft; Baiwen Zhao for formal analysis, validation; Juliana F. de Lima for conceptualization, writing-review and editing; Richard I. Walton for formal analysis funding, writing-review and editing; Osvaldo Antonio Serra for conceptualization, project administration, resources, software, validation, visualization, writing-review and editing.

References

1. Furukawa, H.; Cordova, K. E.; O'Keeffe, M.; *Science* **2013**, *341*, 974. [Crossref]
2. Li, H.; Eddaoudi, M.; O'Keeffe, M.; Yaghi, O. M.; *Nature* **1999**, *402*, 276. [Crossref]
3. Hussain, M. Z.; Pawar, G. S.; Huang, Z.; Tahir, A. A.; Fischer, R. A.; Zhu, Y.; Xia, Y.; *Carbon* **2019**, *146*, 348. [Crossref]
4. Cao, X.; Tan, C.; Sindoro, M.; Zhang, H.; *Chem. Soc. Rev.* **2017**, *10*, 2677. [Crossref]
5. Huang, Z.; Yang, Z.; Hussain, M.Z.; Chen, B.; Jia, Q.; Zhu, Y.; Xia, Y.; *Electrochim. Acta* **2020**, *330*, 135335. [Crossref]
6. Sun, W.; Li, X.; Sun, C.; Huang, Z.; Xu, H.; Shen, W.; *Catalysts* **2019**, *9*, 682. [Crossref]
7. Trovarelli, A.; *Catal. Rev.: Sci. Eng.* **1996**, *38*, 439. [Crossref]
8. Kurian, M.; *J. Environ. Chem. Eng.* **2021**, *8*, 104439. [Crossref]
9. Bugayeva, N.; Robinson, J.; *J. Mater. Sci.* **2007**, *23*, 237. [Crossref]
10. Neha, N.; Prasad, R.; Singh, S. V.; *Bull. Chem. React. Eng. Catal.* **2020**, *15*, 490. [Crossref]
11. Rosado, T. F.; Teixeira, M. P.; Moraes, L. C.; da Silva, L. A.; Silva, A. V. P.; Taylor, J. T.; de Freitas, I. S.; de Oliveira, D. C.; Gardener, J.; Solórzano, G.; Alves, T. V.; Venancio, M. F.; da Silva, M. I. P.; Brocchi, E.; Fajardo, H. V.; da Silva, A. G. M.; *Appl. Catal., A* **2021**, *613*, 118010. [Crossref]
12. Wu, M.; Li, W.; Ogunbiyi, A. T.; Guo, G.; Xue, F.; Chen, K.; Zhang, B.; *ChemCatChem*. **2021**, *13*, 664. [Crossref]
13. Li, S.; Lu, X.; Shi, S.; Chen, L.; Wang, Z.; Zhao, Y.; *Front. Chem.* **2020**, *8*, 348. [Crossref]
14. Haftbaradaran, H.; Mossaiby, F.; *Scr. Mater*. **2016**, *114*, 142. [Crossref]
15. Younis, A.; Loucif, A.; *Ceram. Int.* **2021**, *47*, 15500. [Crossref]
16. Magdalane, C. M.; Kaviyarasu, K.; Priyadharsini, G. M. A.; Bashir, A. K. H.; Mayedwa, N.; Matinise, N.; Isaev, A. B.; Al-Dhabi, N. A.; Arasu, M. V.; Arokiyaraj, S.; Kennedy, J.; Maaza, M.; *J. Mater. Res. Technol.* **2019**, *8*, 2892. [Crossref]
17. Ameur, N.; Fandi, Z.; Taieb-Brahimi, F.; Ferouani, G.; Bedrane, S.; Bachir, R.; *Appl. Phys. A* **2021**, *127*, 162. [Crossref]
18. Wang, J.; Cao, Z.; Feng, M.; Zhang, G.; Yu, B.; *J. Mater. Sci.: Mater. Electron*. **2018**, *29*, 3730. [Crossref]

19. Yu, T.; Lim, B.; Xia, Y. N.; *Angew. Chem., Int. Ed.* **2010**, *49*, 4484. [Crossref]
20. Feng, Z.; Zhang, M.; Ren, Q.; Mo, S.; Peng, R.; Yan, D.; Fu, M.; Chen, L.; Wu, J.; Ye, D.; *Chem. Eng. J.* **2019**, *369*, 18. [Crossref]
21. Yildirim, S.; Akalin, S. A.; Oguzlar, S.; Ongun, M. Z.; Ozer, C.; Erol, M.; *J. Mater. Sci.: Mater. Electron.* **2019**, *30*, 13749. [Crossref]
22. dos Santos, A. P. B.; Dantas, T. C. M.; Costa, J. A. P.; Souza, L. D.; Soares, J. M.; Caldeira, V. P. S.; Araújo, A. S.; Santos, A. G. D.; *Surf. Interfaces* **2020**, *21*, 1007462. [Crossref]
23. Annis, J. W.; Fisher, J. M.; Thompsett, D.; Walton, R. I.; *Inorganics* **2021**, *9*, 40. [Crossref]
24. Wang, H.; Jie Zhu, J.; Min Zhu, J.; Hong Liao, X.; Xu, S.; Dinga, T.; Yuan Chen, H.; *Phys. Chem. Chem. Phys.* **2002**, *4*, 3794. [Crossref]
25. Chen, G.; Guo, Z.; Zhao, W.; Gao, D.; Li, C.; Ye, C.; Sun, G.; *ACS Appl. Mater. Interfaces* **2017**, *9*, 39594. [Crossref]
26. Geranmayeh, S.; Mohammadnezhad, F.; Abbasi, A.; *J. Inorg. Organomet. Polym. Mater*. **2016**, *26*, 109. [Crossref]
27. Zhu, X.; He, H.; Li, Y.; Wu, H.; Fu, M.; Ye, D.; Wu, J.; Huang, H.; Hu, Y.; Niu, X.; *Nanomaterials* **2020**, *10*, 983. [Crossref]
28. Chen, Z.; Chen, Z.; Farha, O. K.; Chapman, K. W.; *J. Am. Chem. Soc*. **2021**, *143*, 8976. [Crossref]
29. Lu Sun, J.; Zhen Chen, Y.; Di Ge, B.; Hua Li, J.; Ming Wang, G.; *ACS Appl. Mater. Interfaces* **2019**, *11*, 940. [Crossref]
30. Nozza, E.; Valentini, S.; Melzi, G.; Vecchi, R.; Corsini, E.; *Sci. Total Environ*. **2021**, *780*, 146391. [Crossref]
31. Niu, X.; Jones, T.; BéruBé, K.; Chi Chuang, H.; Sun, J.; Ho, K. F.; *Sci. Total Environ*. **2021**, *767*, 144391. [Crossref]
32. Xiong, Y.; Chen, S.; Ye, F.; Su, L.; Zhang, C.; Shen, S.; Zhao, S.; *Chem. Commun.* **2015**, *51*, 4635. [Crossref]
33. Wen, Y. H.; Cheng, J. K.; Feng, Y. L.; Zhang, J.; Li, Z. J.; Yao, Y. G.; *CCDC 290771, Experimental Crystal Structure Determination*; Cambridge Crystallographic Data Centre, 2006. [Crossref]
34. Calvache-Muñoz, J.; Prado, F. A.; Tirado, L.; Daza-Gomez, L. C.; Cuervo-Ochoa, G.; Calambas, H. L.; Rodríguez-Páez, J. E.; *J. Inorg. Organomet. Polym. Mater.* **2019**, *29*, 813. [Crossref]
35. Lykaki, M.; Stefa, S.; Carabineiro, S. A. C.; Pandis, P. K.; Stathopoulos, V. N.; Konsolakis, M.; *Catalysts* **2019**, *9*, 371. [Crossref]
36. Zhang, S.; Lee, J.; Kim, D. H.; Kim, T.; *Mol. Catal.* **2020**, *482*, 110703. [Crossref]
37. Nascimento, L. F.; Lima, J. F.; de Sousa Filho, P. C.; Serra, O. A.; *Chem. Eng. J.* **2016**, *290*, 454. [Crossref]
38. Liu, P.; Niu, R.; Li, W.; Wang, S.; Li, J.; *Catal. Lett.* **2019**, *149*, 1007. [Crossref]
39. Zhu, H.; Qin, Z.; Shan, W.; Shen, W.; Wang, J.; *J. Catal.* **2004**, *225*, 267. [Crossref]
40. Zhang, W.; Niu, X.; Chen, L.; Yuan, F.; Zhu, Y.; *Sci. Rep.* **2016**, *6*, 29062. [Crossref]
41. Loridant, S.; *Catal. Today* **2021**, *373*, 98. [Crossref]
42. Bera, P.; Anandana, C.; *RSC Adv.* **2014**, *108*, 62935. [Crossref]
43. Burroughs, P.; Hamnett, A.; Orchard, A. F.; Thornton, G. J.; *J. Chem. Soc., Dalton Trans*. **1976**, *17*, 1686. [Crossref]
44. Praline, G.; Koel, B. E.; Hance, R. L.; Lee, H. I.; White, J. M.; *J. Electron Spectrosc. Relat. Phenom.* **1980**, *21*, 17. [Crossref]
45. Bêche, E.; Charvin, P.; Perarnau, D.; Abanades, S.; Flamant, G.; *Surf. Interface Anal.* **2018**, *40*, 264. [Crossref]
46. Zhang, J.; Wong, H.; Yu, D.; Kakushima, K.; Iwai, H.; *AIP Adv.* **2014**, *4*, 117117. [Crossref]
47. Gupta, A.; Das, S.; Neal, C. J.; Seal, S.; *J. Mater. Chem. B* **2016**, *19*, 3195. [Crossref]
48. Nascimento, L. F.; Lima, J. F.; Souza Filho, P. C.; Serra, O. A.; *J. Environ. Sci.* **2018**, *73*, 58. [Crossref]
49. Aneggi, E.; Wiater, D.; de Leitenburg, C.; Llorca, J.; Trovarelli, A.; *ACS Catal.* **2014**, *4*, 172. [Crossref]
50. Chen, Z.; Chen, L.; Jiang, M.; Gao, X.; Huang, M.; Li, Y.; Ren, L.; Yang, Y.; Yang, Z.; *Appl. Surf. Sci.* **2020**, *510*, 145401. [Crossref]
51. Tsai, Y. C.; Lee, J.; Kwon, E.; Huang, C. W.; Huy, N. N.; You, S.; Hsu, P. S.; Oh, W. D.; Lin, K. Y. A.; *Catalysts* **2021**, *11*, 1128. [Crossref]
52. Li, B.; Raj, A.; Croiset, E.; Wen, J. Z.; *Catalysts* **2019**, *9*, 815. [Crossref]
53. Li, S.; Yan, S.; Xia, Y.; Cui, B.; Pu, Y.; Ye, Y.; Wang, D.; Liu, Y. Q.; Chen, B.; *Appl. Catal., A* **2019**, *570*, 299. [Crossref]

Submitted: February 22, 2024